

A Finite-Element Model Showing Increased Carrier Mobility in Downscaled Amorphous Semiconductors for Flexible Microprocessors

Yuezhou Luo, and Andrew John Flewitt

Abstract—It is shown that the carrier mobilities of amorphous semiconductors can be significantly increased through device downscaling without material-level optimization. This is based on a recently published scalable finite-element model for amorphous semiconductors. Using hydrogenated amorphous silicon (a -Si:H) in an ideal field effect transistor (FET) as an example, the intrinsic DC electron mobility at room temperature is estimated to increase by a factor of at least 8.33 when the channel length is decreased to 10 nm. Keeping a sufficient channel width ensures device-to-device (D2D) uniformity. The simulation is based on the multiple trapping and release (MTR) theory in combination with statistical equivalent analyses. The increased mobility is attributed to the short channel length relative to the characteristic length scale of band fluctuation that is determined by the medium-range order of the material. This paper may inspire the development of next-generation high-density, high-speed, flexible microprocessors based on low-cost amorphous semiconductors for Internet of Things devices.

Index Terms— Amorphous semiconductors, downscaling, carrier mobility, band structure, charge transport

I. Introduction

As a result of the demands for superior flexible electronics in Internet of Things (IoT) devices, there is an increasing interest in merging “mainstream” integrated circuits (where high speed and high density are desired) with large-area electronics based on non-crystalline thin film semiconductors (where low cost and excellent flexibility stand out) [1-4]. A great barrier, however, is the low carrier mobility of these non-crystalline materials compared with their crystalline counterparts. Taking amorphous semiconductors as an example, the disorder-induced band tails in the density of states (DOS) distribution act as a major factor that limits carrier mobility due to carrier localization.

This is the full-length version of the paper that has been submitted to the IEEE for possible publication. Copyright may be transferred without notice, after which this version may no longer be accessible. This work is supported by the UKRI Engineering and Physical Sciences Research Council (EP/W009757/1), the Rank Prize Return to Research Grant, and the Cambridge Commonwealth, European and International Trust Ph.D. scholarship. (Corresponding author: Yuezhou Luo)

Yuezhou Luo and Andrew John Flewitt are with the Electrical Engineering Division, Department of Engineering, University of Cambridge, Cambridge CB3 0FA, UK (e-mail: YL778@cam.ac.uk).

Licensed under CC BY 4.0, the supporting data for this article will be openly available from the University of Cambridge repository (Apollo) once this manuscript is accepted for publication.

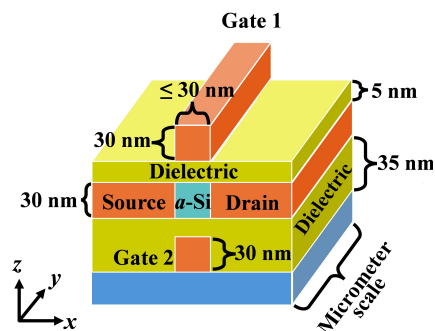


Fig. 1. Strictly downscaled dual-gate field effect transistor (FET). The carrier channel length is strictly equal to the source-drain separation.

In the first prequel to this paper (henceforth named Paper I [5]) which is recently published, we used hydrogenated amorphous silicon (a -Si:H) as an example and reinvestigated the essence of localized band tail states from the perspective of excess delocalized charges, which induce extra potentials that force the crystalline silicon (c -Si) band edge to fluctuate in the energy-space diagram. Such a band fluctuation may be decomposed into various components using Fourier transform analysis; the dominant ones are of low spatial frequencies. In our model, the length scales of these dominant components are typically ≥ 30 nm as determined by the specific medium-range order (MRO). Band fluctuation below this scale would thus be confined to a narrower energy range; a -Si:H would then be progressively more electronically like c -Si as the scale reduces, featuring fewer localized band tail states and a higher mobility.

As is the trend in the general microelectronics industry, downscaling has also received much attention in the field of thin film transistors (TFTs) based on amorphous semiconductors. Contrarily, existing studies do not straightforwardly corroborate our hypothesis above (e.g., Refs. [6-8]). We highlight that this is mainly due to the interference of contact resistances, and also the staggered TFT structure used, where the actual carrier channel is partly correlated with the unscaled gate length, and is thus longer than the downscaled source-drain separation. The mobility characterized in this setting does not authentically reflect the actual mobility in the downscaled region, so this paper looks into a controlled device.

II. DEVICE STRUCTURE AND AVERAGE DC MOBILITY

In Fig. 1, the metal source and drain of an ideal dual-gate field effect transistor (FET) are separated by ≤ 30 nm; their width and thickness are standard. a -Si:H exists only inside the gap, so the carrier channel length is strictly downscaled, which we term *strict downscaling*. The dual-gate structure is proposed

to enhance gate controllability in such an ultra-scaled setting. Fabrication of this FET can be done similar to the processes described in Ref. [9].

Many previous studies of TFTs focused on the apparent field effect mobility, which, as mentioned earlier, can be heavily affected by non-ideality factors such as contact resistance. We believe that these non-ideality factors may be eventually mitigated and optimized using existing strategies, whereas it is the intrinsic material property that has not been thoroughly investigated. To validate our hypothesis, this paper thus focuses on the intrinsic DC carrier mobility under a zero gate bias.

In practical scenarios, the FET works under a very low drain-source voltage compared with ordinary macroscopic TFTs such that the source-drain electric field in the channel maintains a typical magnitude. For conduction in *a*-Si:H, electron carriers play a much more important role than holes [10]. The scattering-induced thermal motion of these electron carriers adds noise that does not contribute to net conduction, so an imagined *drift center* is introduced to describe the net drift motion of every electron carrier. When the drift centers are near the metal-semiconductor interfaces, there is a complexity that electrons may be in the metals while their drift centers are in the *a*-Si:H. To exclude this complexity, a region named **R** within *a*-Si:H is defined which is kept slightly away from the source and drain electrodes but which still reliably represents the entire *a*-Si:H; this is shown in Fig. 2(a).

It is assumed that, after applying the drain-source voltage, the DC conduction lasts for a sufficiently long time T_0 relative to the time t_0 for the system to reach a steady current I_{SS} . The average conductivity $\bar{\sigma}$ of **R** is thus

$$\bar{\sigma} = \frac{I_{SS}b}{U_R S}, \quad (1)$$

where b is the length of **R**, S is the cross-sectional area of the device, and U_R is the voltage across **R**. It should be noted that a reliably measured I_{SS} is deemed as the *net current* that is contributed only by the drift motion of electrons and is exclusive of noise caused by random thermal motion; it can therefore be calculated as

$$I_{SS} = \frac{eN_d}{T_0}. \quad (2)$$

Here, e is the elementary charge and N_d denotes the total number of drift centers that have passed through **R** within T_0 .

The number of electron carriers inside **R** after time t_0 is statistically fluctuating around \bar{N} which is

$$\bar{N} = bS \int_{E_L}^{+\infty} g(E) f(E) dE, \quad (3)$$

where $g(E)$ is the DOS distribution of the entire *a*-Si:H inside **R**, E_L is the bottom of the conduction band (CB) tail, and $f(E)$ is the Fermi-Dirac distribution. The statistical fluctuation around \bar{N} is caused by three factors. First, from the energy perspective, electrons randomly occupy all possible electronic states. The noise brought by this occupation randomness has been filtered using the Fermi-Dirac statistics. Second, from the spatial perspective, the dynamic random motion of electrons leads to additional fluctuation noise; this has been filtered using the drift center concept. Third, from the temporal perspective, due to the fact that N is far less than unity considering the nanoscale b , the actual number of drift centers within **R** is

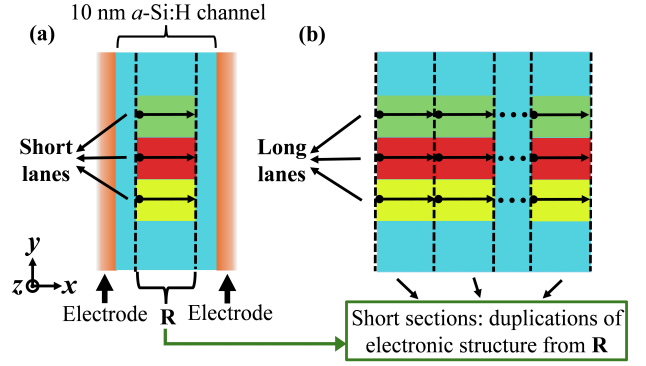


Fig. 2. Discretized transport analysis and its equivalence. (a) An illustration of the division of lanes in **R** perpendicular to the x axis (z -direction division not shown). Each lane is given a specific color to demonstrate its unique local electronic structure. The motion of the drift centers of electron carriers are illustrated by the black arrows. (b) A virtual thin film constructed by duplicating the electronic structures of **R** for numerous times along the x axis.

temporally varying between 0 and 1. To filter the third fluctuation, we observe **R** throughout T_0 which is sufficiently long. Suppose that the drift center of the i^{th} of the N_d electrons drifts across **R** for a duration t_i , where

$$t_i = \frac{b}{v_i} = \frac{b^2}{\mu_i U_R}, \quad (4)$$

with $i \in [1, N_d]$, v_i being the average velocity of the drift center as it crosses **R**, and μ_i being the corresponding mobility. The temporal perspective shows that the cumulation of the drift time of all these N_d electrons is equal to NT_0 . Thus,

$$\sum_{i=1}^{N_d} t_i = \bar{N} T_0. \quad (5)$$

Substituting (2) and (4) into (5) yields

$$\sum_{i=1}^{N_d} \frac{b^2}{\mu_i U_R} = \bar{N} \frac{eN_d}{I_{SS}}. \quad (6)$$

The average electron mobility of **R**, which represents the mobility of the entire *a*-Si:H, is defined by (1) and (3) as

$$\bar{\mu} = \frac{I_{SS}b}{U_R S} / \frac{e\bar{N}}{bS}, \quad (7)$$

integrating which into (6) leads to

$$\bar{\mu} = N_d / \sum_{i=1}^{N_d} (1/\mu_i). \quad (8)$$

III. EQUIVALENT TRANSPORT ANALYSIS

The second prequel to this paper (henceforth named Paper II [11]) revisited and modified multiple trapping and release (MTR) transport, which is the predominant charge transport mechanism of room-temperature *a*-Si:H [12] (and many other amorphous semiconductors). For a macroscale *a*-Si:H thin film, the average DC conductivity mobility of electrons is

$$\mu_a = \mu_{Ceff} \frac{n_{ext,eff}}{n_{ext,eff} + n_{loc,eff}}, \quad (9)$$

where μ_{Ceff} is the effective extended-state mobility. $n_{ext,eff}$ and $n_{loc,eff}$ respectively denote the densities of electrons that are in effective extended states and effective localized states,

demarcated by the effective CB mobility edge E_{Ceff} , these densities are calculated based on the inner product of the DOS distribution and Fermi distribution.

Direct evaluation of mobility via (9) is valid only when both of the following assumptions are true. First, uniformity. Extended states and localized states are approximately uniform in space such that all carriers end up interacting with generally similar electronic structures. Second, sufficiency. Carriers undergo numerous trapping and release events during their migration to allow the exhibition of statistical nature. These two assumptions cease to hold true as a -Si:H downscales. It is most evident that the sufficiency assumption collapses as it is unlikely for an electron to undergo multiple trapping and release events during its ultra-short migration time across the short channel. The uniformity assumption also no longer holds true. Although there is macroscopic uniformity along the y axis, the dimension along the x axis is too small to exhibit any macroscopic attributes. Unlike in a large film where the random motion of electrons may accumulate laterally, electrons in \mathbf{R} migrate along the x axis predominantly due to the ultra-short migration duration, and so their y and z coordinates vary trivially. Consequently, electrons that are well-separated along the y axis may end up interacting with significantly different electronic structures at these locations.

To tackle this problem, in Fig. 2(a), \mathbf{R} is *virtually* divided along the y and z axis into N_\perp “lanes” with a reasonable cross section. Since electrons predominantly move along the x axis and stay in the vicinity of their drift centers, it is reasonable to adopt discretization and treat electrons as being confined in the lanes where their drift centers locate. The determination of the lane cross section is based on two qualitative criteria.

- (1) The lanes must be narrow enough such that in any lane the band fluctuation along the y axis is not significant and that all electrons within the same lane interact with almost the same electronic structures.
- (2) The lanes must not be too narrow and should accommodate the typical range of the lateral thermal motion of electrons in \mathbf{R} .

Assume that throughout T_0 there are totally n_s drift centers that migrate across \mathbf{R} along the s^{th} lane, the j^{th} of which exists in \mathbf{R} for a duration $t_{s,j}$ and exhibits a mobility of $\mu_{s,j}$ with $j \in [1, n_s]$.

$$\sum_{j=1}^{n_s} t_{s,j} = N_s T_0, \quad (10)$$

where N_s is the average number of drift centers inside the s^{th} lane. This is quantified by

$$N_s = (bS / N_\perp) \int_{E_{Ls}}^{+\infty} g_s(E) f(E) dE, \quad (11)$$

where $g_s(E)$ is the local DOS distribution of the s^{th} lane, and E_{Ls} is the bottom of the CB tail of the s^{th} lane.

Neglecting the influence of thermal fluctuations in the material on the motion of individual drift centers, basic statistics reveals that the migrations of these n_s drift centers are *independent random experiments*, while the drift time (thus the mobilities) of these electrons are *outcomes*. As electrons are indistinguishable, it is equivalent to conduct these random experiments using a single electron; this corresponds to a scenario where a single drift center migrates across \mathbf{R} along the same lane for n_s times. This scenario is produced virtually. In

Fig. 2(b), the *electronic structures* (not the material) in \mathbf{R} are duplicated M times along the x axis, where, for $\forall s \in [1, N_\perp]$, $M > n_s$. A “virtual thin film” forms, which comprises “long lanes” duplicated from the electronic structure of the corresponding short lanes in Fig. 2(a). The statistical equivalence of “the repeated drift of the single electron across \mathbf{R} for n_s times” is now “the drift of the single electron across n_s short sections in a long lane of the virtual thin film”, under the same electric field.

In Fig. 2(b), the electron requires a time $t_{s,k}$ to cross the k^{th} section in the s^{th} long lane and exhibits a mobility $\mu_{s,k}$, with $k \in [1, n_s]$. Given the equivalence and the sufficiently large n_s ,

$$\sum_{k=1}^{n_s} t_{s,k} = \sum_{j=1}^{n_s} t_{s,j}, \quad (12)$$

with both equal to $N_s T_0$ considering (10). Multiplying both sides of (12) by U_R/b^2 where U_R is the voltage across \mathbf{R} ,

$$\sum_{k=1}^{n_s} (1/\mu_{s,k}) = \sum_{j=1}^{n_s} (1/\mu_{s,j}). \quad (13)$$

The average mobility exhibited by the electron after it has migrated across the first n_s short sections in the virtual thin film

is a harmonic mean $n_s / \sum_{k=1}^{n_s} (1/\mu_{s,k})$. Since n_s is large, this

average mobility is statistically equal to the average electron mobility of the entire long lane in the virtual thin film; this *lane mobility* is denoted as $\bar{\mu}_s$ and can now be quantified by (9).

Including this into (13) and combining (8), the mobility of \mathbf{R} is

$$\bar{\mu} = \left(\sum_{s=1}^{N_\perp} n_s \right) / \sum_{s=1}^{N_\perp} (n_s / \bar{\mu}_s). \quad (14)$$

It should be noted that considering the migration distance,

$$\bar{\mu}_s \mathcal{E} \sum_{k=1}^{n_s} t_{s,k} = n_s b, \quad (15)$$

where it is assumed that the electric field \mathcal{E} ($= U_R/b$) is uniform within \mathbf{R} . Eqs. (10), (12) and (15) simplify (14) to

$$\bar{\mu} = \sum_{s=1}^{N_\perp} N_s \bar{\mu}_s / \sum_{s=1}^{N_\perp} N_s. \quad (16)$$

IV. SIMULATION

As a comparative study, we base this paper on the 2.5D excess delocalized charge model developed in Paper I [5]. This model approximates a standard defect-free a -Si:H thin film, whose electron mobility is to be compared with that after downscaling. Note that due to computational cost, the 2.5 model is only 150-nm long (rather than in the micrometer scale which is the actual situation). Hence, to produce a sufficient contrast in the channel length, downscaling to 10 nm is simulated. It should be mentioned that the actual material deposition conditions are the same regardless of the length, and so the extent of bond angle and bond length distortion, which determines the excess delocalized charges, is the same in both cases. Thus, assuming that the metal-semiconductor interfacial charges are trivial, the downscaled a -Si:H is simply a “strip” from the 2.5D excess delocalized charge model [Fig. 3(a)].

As the first trial, we extract a strip between $x = 100a_0$ and $x = 133a_0$ from the original 2.5D model. Here, $a_0 = 3 \text{ \AA}$ is the typical short-range order length in a -Si:H (details, see Paper I).

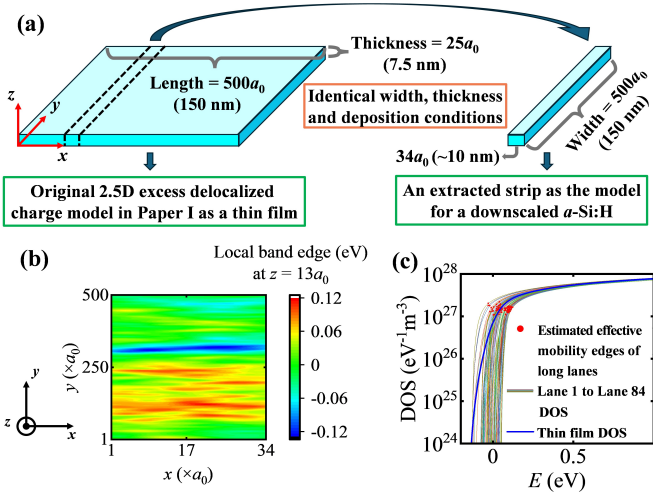


Fig. 3. Mobility after downscaling. (a) Modeling the downscaled *a*-Si:H based on the 2.5-dimensional (2.5D) model in Paper I [5]. (b) The band edge distribution in the middle layer of the downscaled *a*-Si:H. (c) The density of states (DOS) distributions of the long lanes in the virtual thin film. The DOS of the original 2.5D model is compared. The red dots denote the overestimated effective mobility edges.

The band edge distribution at the $z = 13a_0$ layer is mapped in Fig. 3(b) in a stretched fashion for a better presentation which also highlights the highly directional electron migration. The typical spatial range of an electron away from its drift center during its migration is reasonably estimated to be $6a_0$ given the typical atomic-spacing-scale scattering length of free electrons in *a*-Si:H [10, 11, 13] and the picosecond-scale transit time under a typical 40 kV cm^{-1} measurement field [12]. \mathbf{R} is thus defined as a $21a_0$ -long region in the downscaled *a*-Si:H, leaving $\sim 6a_0$ -long regions on both sides. \mathbf{R} is then virtually divided into 84 narrow lanes; their cross section is $\sim 12a_0 \times 12a_0$.

The DOS distributions of long lanes in the virtual thin film are easily calculated based on Fig. 3(b) using the method in Paper I [5]; these are shown in Fig. 3(c). To evaluate $\bar{\mu}_s$ of a lane at room temperature using (9), the effective mobility edge E_{Ceff} of the lane needs to be known. A worst-case scenario is

considered; E_{Ceff} is overestimated to be at the highest local band edge in the lane. The effective extended-state mobility μ_{Ceff} is also needed. According to Eq. (30) in Paper II [11], μ_{Ceff} is a complex outcome of the actual free electron mobility (μ_0) determined by carrier scattering, and a band structure factor ($n_{loc,eff}/n_{ext,eff}$). On the one hand, as evident in Fig. 3(b), the reduced density of localized states in individual lanes tends to decrease the latter factor. On the other hand, a more uniform energy distribution of band edges in the individual lanes than that in the macroscopic film tends to weaken electron scattering and thereby increases μ_0 . These two mechanisms tend to cancel each other, so it is reasonable to treat the μ_{Ceff} of the lanes to be similar to that of the macroscopic film before downscaling. Then, based on (16), the intrinsic DC mobility after downscaling is $8.83 \text{ cm}^2/(\text{V s})$, 8.33 times the mobility before downscaling [11, 14]. Note that the dependence of this result on the Fermi level position (thus the FET gate voltage) is trivial, which fundamentally results from the assumption of trivial defect states such that the changes of $n_{ext,eff}$ and $n_{loc,eff}$ in (9) with Fermi level are almost synchronous and cancel each other.

As illustrated in Fig. 4(a), device-to-device (D2D) variation is investigated after conducting five more trials through extracting charges at randomly chosen x positions from the original 2.5D model. They are at $[50a_0, 83a_0]$, $[200a_0, 233a_0]$, $[290a_0, 323a_0]$, $[350a_0, 383a_0]$ and $[420a_0, 453a_0]$, respectively. The 8.33-time improvement turns out to be the worst case among the six trials. The coefficient of variation (CV) of the mobilities of the six trials is 17.22%. To qualitatively make sense of this value, the variation of the 84 lane mobilities ($\bar{\mu}_s$) within each single trial is investigated as a comparison. Results in Fig. 4(c) show that for any of these six trials, the $\bar{\mu}_s$ variation of the 84 lanes is significantly higher than 17.22%. In another word, \mathbf{R} as a whole is less prone to vary in properties than its internal lanes. This demonstrates that keeping a sufficient device width is crucial in suppressing variations, which is due to the weighted mean operation in (16) and the weak correlation between N_s and $\bar{\mu}_s$ as shown in Fig. 4(d). In addition to the

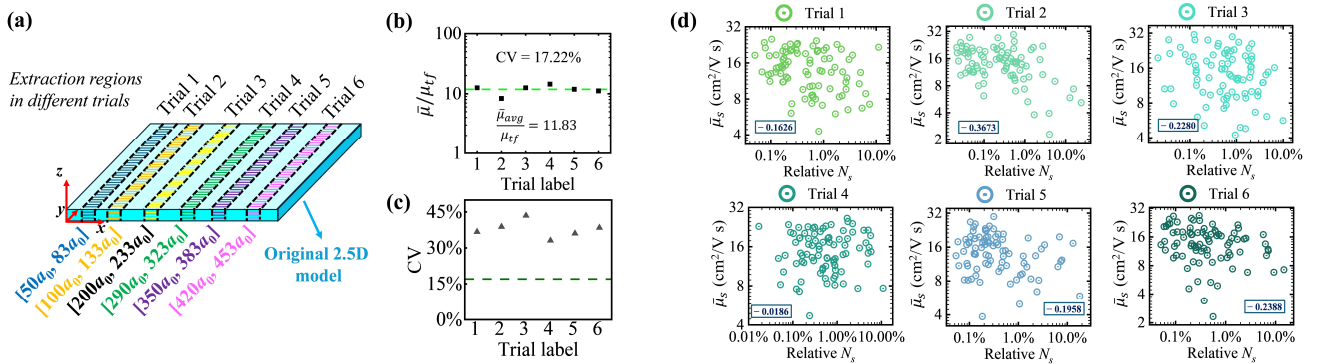


Fig. 4. Device-to-device (D2D) variation. (a) An illustration of the production of the six random trials. For each trial, the extraction region along the x axis of the original 2.5-dimensional (2.5D) thin film model is indicated in a unique color. (b) Mobility variation. The average mobility of the six trials is 11.83 times the mobility (μ_H) of their thin film counterpart (dashed green line). The coefficient of variation (CV), which reflects the D2D variation, is 17.22%. (c) The CV of the 84 lane mobilities ($\bar{\mu}_s$) in each of the six trials. These CVs (black triangles) are significantly higher than 17.22% (dashed olive line), indicating that the large width-to-length (W/L) ratio of the proposed device facilitates the decrease of D2D variation. (d) Correlation between the number of drift centers (N_s) inside a lane of \mathbf{R} and the corresponding lane mobility ($\bar{\mu}_s$) in Fig. 2(b). All the six random trials are investigated. The relative N_s [i.e., the weight in Eq. (16)] is obtained through dividing N_s by the sum of N_s of the 84 lanes in \mathbf{R} . The correlation between $\bar{\mu}_s$ and the relative N_s is weak, as revealed by the Pearson coefficients in the indigo frames in the figures. Logarithmic scales are adopted.

intrinsic mobility, in real devices, the D2D variation also depends on the variation of metal-semiconductor contact resistance. Ensuring a sufficient width is, again, crucial. It is evident that the local contact resistance at a specific lane depends on the difference between the metal Fermi level and the a -Si:H band edge at this lane near the interface, but the overall contact resistance across the entire interface is averaged from all lanes. Given that the band edge distribution along the interface is random in the long range, the contact resistance must therefore be highly invariant for the proposed structure. In reality, the D2D variation must be even lower than the simulation results here because the actual width will be in micrometer scales, far exceeding the model scale in this paper.

V. QUALITATIVE UNDERSTANDING OF MOBILITY INCREASE

The virtual thin film in Fig. 2(b) is now named Film I. The purpose of constructing Film I is to equivalently reproduce the repeated drift of electrons across the respective lanes in \mathbf{R} . As analyzed earlier, electrons are treated as being confined in the lanes where their drift centers locate. This consequently leads to the virtual confinement of electrons within the respective long lanes of Film I. The average DC mobility of Film I is thus equal to the average DC mobility of \mathbf{R} , both being quantified by (16). This confinement is in contrast to the situation in a real macroscopic thin film material, where the random thermal motion of electrons may accumulate in the lateral directions significantly, and so electrons could interact with a variety of electronic structures in the material.

The lateral confinement in Film I could be understood, from a physical perspective, as a result of the existence of certain “artificial structures” at the lane boundaries, which has no other effects except elastically scattering electrons. Because of these imagined scattering boundaries, electrons do not have chances to interact with different electronic structures at different lateral positions, so the property of Film I would differ from that of a real thin film. In order to better resemble a real thin film, Film II is produced virtually through randomizing the lateral arrangement of the short sections in Film I. This is illustrated in Fig. 5. Note that similar to the virtual construction of Film I, the virtual construction of Film II also targets the electronic structures, instead of the actual microscopic material structure. In another word, there is no explicit relation between the material structures of \mathbf{R} , Film I and Film II. Despite the confinement, an electron drifting along a specific long lane in Film II has the chance to interact with a variety of electronic structures, which appears similar to the case in a real thin film.

The DOS distribution of any long lane in Film II is identical to that of \mathbf{R} because of the unbiased randomization operation. Considering the sufficient width, it is assumed that the DOS distribution of \mathbf{R} is similar to that of the real thin film. The long lanes in Film II thus share nearly the same DOS distribution with the real thin film. Consequently, the average DC mobility of Film II is deemed being similar to that of the real thin film.

Comparing Film I and II, the lateral randomization of the short sections does not alter their internal mobilities, but nontrivial energy barriers exist in Film II because of the differences in the local electronic structures (denoted by different colors) as a result of the randomization. This leads to a lower average DC mobility of Film II than Film I.

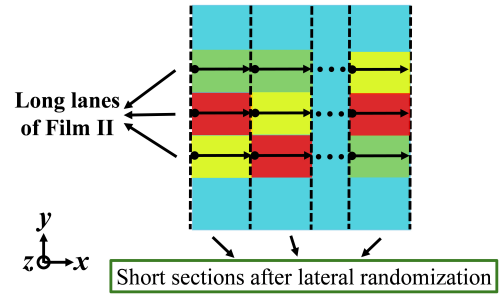


Fig. 5. Construction of Film II through lateral randomization of short sections in Film I.

Consequently, the average DC mobility of \mathbf{R} is higher than that of the thin film before downscaling.

VI. THE ROLE OF MEDIUM-RANGE ORDER

The simulation in Sec. IV is based on the model in Paper I where the medium-range order (MRO) in a -Si:H is quantified by a modeling parameter named window dimension (w) that is chosen to be $5a_0$. In reality, MRO depends on deposition conditions and the resultant film quality. Viewing MRO as a variable, this section considers the results of mobility improvement under various choices of w .

In Paper I, there are four additional choices of w (i.e., $w = 0$, $w = 2a_0$, $w = 10a_0$ and $w = 20a_0$). Accordingly, four additional thin films are modeled based on different distributions of excess delocalized charges. Here, it has been ensured that the

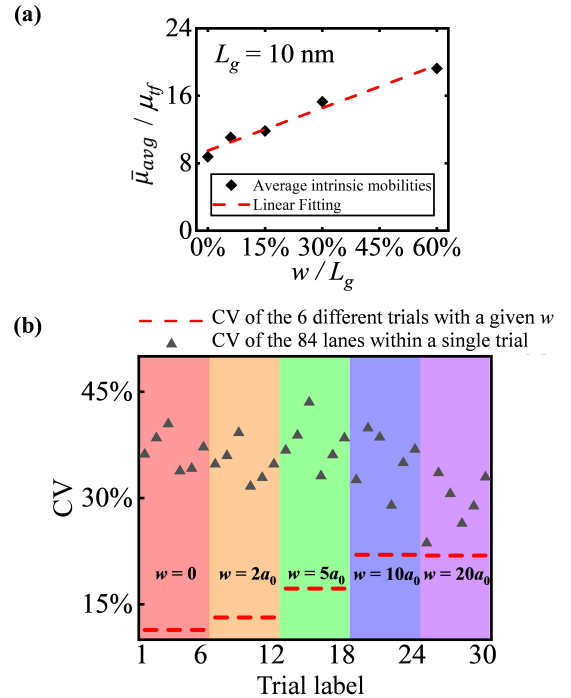


Fig. 6. Investigation of the role of medium-range order. (a) The dependence of the intrinsic mobility on the modeling parameter w in Paper I. For each w , six trials are conducted as before; the average mobility of the six trials is labeled in the figure. (b) The coefficients of variation (CVs) of \mathbf{R} under different w and the CVs of the 84 lanes of \mathbf{R} in individual trials. The CV of \mathbf{R} tends to saturate at $\sim 20\%$ as w increases (dashed red lines). These CVs are significantly lower compared with the variation among the 84 lanes in any of these trials (as labeled by the black triangles).

DOS distributions of these four thin films match experimental DOS data as satisfactorily as the studied $w = 5a_0$ film did. Considering the need to investigate D2D variation, 6 trials are attempted for each of the four films according to the strategies detailed in Sec. IV. Together with the results in Sec. IV, the mobilities of 30 trials in total have been quantitatively evaluated. As revealed by Fig. 6(a), the intrinsic mobility (an average quantity after considering D2D variations) increases nearly linearly with the increase of w under a fixed channel length (L_g). Therefore, it is the relative length scale of the channel compared to the MRO length that fundamentally determines the intrinsic mobility. The change of channel length under a fixed MRO would therefore also alter the intrinsic mobility. This is, however, not quantitatively investigated at the moment, because changing channel length inevitably changes the cross section of the divided lanes due to the different extents of electron lateral span; a precise quantification of this effect is currently unknown. Nevertheless, the significant mobility improvement simulated at the 10-nm scale in this paper is a highly convincing proof that similar mobility improvement should also exist at slightly longer scales (e.g., 30 nm, as indicated in Sec. I). There might be concerns on the gate controllability as well as the risk of source-to-drain tunneling at the extreme 10-nm scale, but these concerns should fall away when the scale slightly increases to ~ 30 nm (e.g., Ref. [9]).

In Fig. 6(b), the 30 trials are labeled in such a way that “Trial r ” to “Trial $6r$ ” denote the six trials for the r^{th} 2.5D thin film model, where r respectively equals to 1, 2, 3, 4 and 5 for the thin film whose w is 0, $2a_0$, $5a_0$, $10a_0$ and $20a_0$. It is shown that the CV of \mathbf{R} tends to saturate at $\sim 20\%$ as the MRO improves. Under any choice of w , the CV of the six trials is significantly lower than the mobility variation among the 84 lanes in any of these six trials. Such a D2D suppression, as analyzed in Sec. IV, would be much more significant in real devices with micrometer-scale widths.

VII. CONCLUSION

In light of our recent breakthroughs in understanding and modeling the band fluctuation in amorphous semiconductors, this paper demonstrates the possibility of using strict downscaling to fundamentally increase the intrinsic carrier mobility of these materials without compromising device-to-device uniformity. Our finite-element model shows a representative mobility improvement of 8.33 times after downscaling an a -Si:H channel to 10 nm. Combined with device-level studies in the future as well as available strategies on the optimization of contact resistance and short channel effects, the work in this paper could eventually lead to the development of next-generation flexible microprocessors with higher density and much better performance.

REFERENCES

- [1] E. Ozer, J. Kufel, J. Myers, J. Biggs, G. Brown, A. Rana, A. Sou, C. Ramsdale, and S. White, "A hardwired machine learning processing engine fabricated with submicron metal-oxide thin-film transistors on a flexible substrate," *Nat. Electron.*, vol. 3, no. 7, pp. 419-425, Jul. 2020, doi: 10.1038/s41928-020-0437-5.
- [2] J. Biggs, J. Myers, J. Kufel, E. Ozer, S. Craske, A. Sou, C. Ramsdale, K. Williamson, R. Price, and S. White, "A natively flexible 32-bit Arm microprocessor," *Nature*, vol. 595, no. 7868, pp. 532-536, Jul. 2021, doi: 10.1038/s41586-021-03625-w.
- [3] H. Oh, J.-Y. Oh, C. W. Park, J.-E. Pi, J.-H. Yang, and C.-S. Hwang, "High density integration of stretchable inorganic thin film transistors with excellent performance and reliability," *Nat. Commun.*, vol. 13, no. 1, p. 4963, Aug. 2022, doi: 10.1038/s41467-022-32672-8.
- [4] W. Wang, K. Li, J. Lan, M. Shen, Z. Wang, X. Feng, H. Yu, K. Chen, J. Li, and F. Zhou, "CMOS backend-of-line compatible memory array and logic circuitries enabled by high performance atomic layer deposited ZnO thin-film transistor," *Nat. Commun.*, vol. 14, no. 1, p. 6079, Sep. 2023, doi: 10.1038/s41467-023-41868-5.
- [5] Y. Luo and A. Flewitt, "Understanding localized states in the band tails of amorphous semiconductors exemplified by a -Si:H from the perspective of excess delocalized charges," *Phys. Rev. B*, vol. 109, no. 10, p. 16, Mar. 2024, doi: 10.1103/PhysRevB.109.104203.
- [6] M. Kim, J. H. Jeong, H. J. Lee, T. K. Ahn, H. S. Shin, J.-S. Park, J. K. Jeong, Y.-G. Mo, and H. D. Kim, "High mobility bottom gate InGaZnO thin film transistors with Si O x etch stopper," *Appl. Phys. Lett.*, vol. 90, no. 21, p. 212114, May. 2007, doi: 10.1063/1.2742790.
- [7] I. Song, S. Kim, H. Yin, C. J. Kim, J. Park, S. Kim, H. S. Choi, E. Lee, and Y. Park, "Short channel characteristics of gallium-indium-zinc-oxide thin film transistors for three-dimensional stacking memory," *IEEE Electron Device Lett.*, vol. 29, no. 6, pp. 549-552, Jun. 2008, doi: 10.1109/LED.2008.920965.
- [8] J. Guo, K. Han, S. Subhechha, X. Duan, Q. Chen, D. Geng, S. Huang, L. Xu, J. An, and G. S. Kar, "A new surface potential and physics based compact model for a-IGZO TFTs at multianoscale for high retention and low-power DRAM application," in *2021 IEEE International Electron Devices Meeting (IEDM)*, Dec. 2021: IEEE, pp. 8.5. 1-8.5. 4, doi: 10.1109/IEDM19574.2021.9720700.
- [9] K. Chen, J. Niu, G. Yang, M. Liu, W. Lu, F. Liao, K. Huang, X. Duan, C. Lu, and J. Wang, "Scaling Dual-Gate Ultra-thin a-IGZO FET to 30 nm Channel Length with Record-high G m, max of 559 $\mu\text{S}/\mu\text{m}$ at V DS= 1 V, Record-low DIBL of 10 mV/V and Nearly Ideal SS of 63 mV/dec," in *2022 IEEE Symposium on VLSI Technology and Circuits (VLSI Technology and Circuits)*, 2022: IEEE, pp. 298-299.
- [10] R. A. Street, *Hydrogenated Amorphous Silicon*. New York: Cambridge University Press, 1991.
- [11] Y. Luo and A. Flewitt, "Revisiting the multiple trapping and release electronic transport in amorphous semiconductors exemplified by a -Si:H," (in review, <https://arxiv.org/abs/2408.03678v2>), 2024.
- [12] P. Le Comber and W. Spear, "Electronic transport in amorphous silicon films," *Phys. Rev. Lett.*, vol. 25, no. 8, p. 509, Aug. 1970, doi: 10.1103/PhysRevLett.25.509.
- [13] M. H. Cohen, "Review of the theory of amorphous semiconductors," *J. Non-Cryst. Solids*, vol. 4, pp. 391-409, Apr. 1970, doi: 10.1016/0022-3093(70)90068-2.
- [14] A. Hourd and W. Spear, "Determination of the extended-state electron mobility in a -Si," *Philos. Mag. B*, vol. 51, no. 2, pp. L13-L18, 1985, doi: 10.1080/13642818508240550.